Cell Reports
Physical Science

CellPress
OPEN ACCESS

Article

Tuning interfacial energetics with surface ligands to enhance perovskite solar cell performance

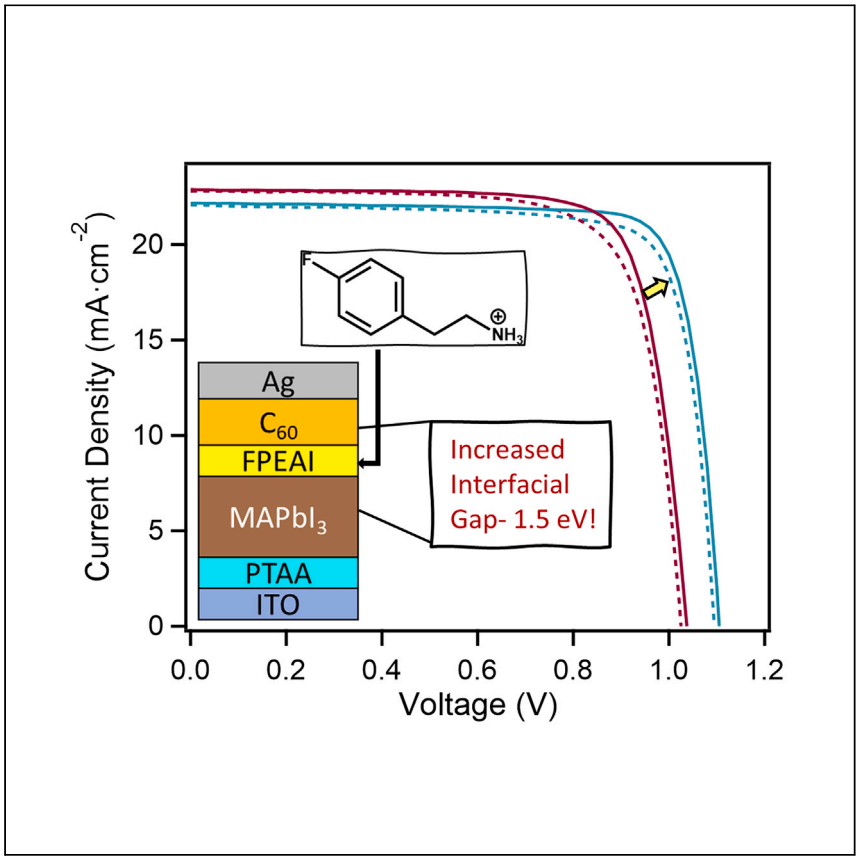

Liu et al. apply surface ligands with varying dipole moments to influence the energy-level alignment between the perovskite and C_{60}. They show that increased perovskite solar cell performance results for surface ligands that maximize this interfacial energy gap, highlighting a key ligand design guideline.

Tuo Liu, Rebecca A. Scheidt, Xiaopeng Zheng, ..., Joseph M. Luther, Matthew C. Beard, Kenneth R. Graham

matt.beard@nrel.gov (M.C.B.)
kenneth.graham@uky.edu (K.R.G.)

Highlights

Surface ligands at perovskite/C_{60} interfaces increase the interfacial energy gap

Recombination rates in perovskite/C_{60} bilayers are independent of the surface ligand

The interfacial energy gap is strongly related to photovoltaic performance

Liu et al., Cell Reports Physical Science 4, 101650
November 15, 2023
https://doi.org/10.1016/j.xcrp.2023.101650

Cell Reports
Physical Science

CellPress
OPEN ACCESS

Article

Tuning interfacial energetics with surface ligands to enhance perovskite solar cell performance

Tuo Liu,[1] Rebecca A. Scheidt,[2] Xiaopeng Zheng,[2] Syed Joy,[1] Qi Jiang,[2] Harindi R. Atapattu,[1] Min Chen,[2] Henry Pruett,[1] Kai Zhu,[2] Joseph M. Luther,[2] Matthew C. Beard,[2,*] and Kenneth R. Graham[1,3,*]

SUMMARY

Surface ligands are often used to improve perovskite solar cells (PSCs). Here, a series of surface ligands with varying dipole moments are applied at the methylammonium lead iodide ($MAPbI_3$)/C_{60} interface to vary the energy-level alignment. All investigated surface ligands improve PSC performance, with 4-fluorophenethylammonium iodide (FPEAI) displaying the greatest improvement. Transient absorption and reflectance measurements show similar recombination dynamics in all ligand-treated $MAPbI_3$/C_{60} bilayer films. Transient photovoltage measurements also show similar recombination lifetimes at similar charge-carrier densities; however, differential capacitance measurements indicate that FPEAI shifts the differential capacitance curve to higher voltages. *In situ* ultraviolet photoemission spectroscopy measurements show that the interfacial energy gap at the $MAPbI_3$/C_{60} interface increases from 1.19 eV with phenethylammonium iodide (PEAI) to 1.50 eV with FPEAI, corresponding to the shift of the differential capacitance curve. This increased interfacial energy gap is responsible for the increased open-circuit voltage (V_{OC}) and should be considered in surface ligand selection.

INTRODUCTION

Metal halide perovskite solar cells (PSCs) have garnered tremendous attention in photovoltaic research due to their low cost and excellent power conversion efficiencies (PCEs), which increased rapidly from 3.8% to 26.0% over the last decade.[1–8] Inverted p-i-n architecture PSCs are regarded as more amenable to low-temperature solution processing, thereby improving the ease at which flexible PSCs and tandem solar cells can be fabricated.[9–11] Thus, the development of inverted PSCs is attracting increasing interest.[12–14]

Interfacial nonradiative recombination and nonoptimal energy-level alignment (ELA) between the perovskite and charge-transport layers are two main factors limiting the PCE of inverted PSCs.[15–19] Previous studies reveal that nonradiative recombination and bending of the quasi-Fermi level splitting (QFLS) at the perovskite/electron transport layer interface significantly decreases the device's open-circuit voltage (V_{OC}) in inverted PSCs.[18,20–22] To increase this interfacial QFLS, strategies such as doping and interface modification are applied to minimize the V_{OC} loss associated with interfacial recombination.[5,17,20–25] The influence of the ELA is more ambiguous, with some results suggesting that the ELA plays a large role and others suggesting that the role of the ELA is more minimal.[14,18,20,21,26]

[1]Department of Chemistry, University of Kentucky, Lexington, KY 40506, USA

[2]National Renewable Energy Lab, Golden, CO 80401, USA

[3]Lead contact

*Correspondence: matt.beard@nrel.gov (M.C.B.), kenneth.graham@uky.edu (K.R.G.)

https://doi.org/10.1016/j.xcrp.2023.101650

Despite interfacial modification being a commonly used method to improve device performance, the details behind how device performance relates to surface ligand structure remain unclear. For example, both electron-withdrawing and -donating groups on the ligands have been shown to improve the performance of n-i-p PSCs, with varying arguments for the mechanism of improvement. In one instance, the addition of electron-donating groups to phenethylammonium iodide (PEAI) improved the PSC performance, which was suggested to arise from increased coordination strength between undercoordinated Pb^{2+} and PEA derivatives with more electron-rich phenyl groups.[27] In another example, extended π-conjugated surface ligands with more electron-donating end groups were observed to result in the largest enhancement of V_{OC} and PCE in p-i-n PSCs.[28] However, in other examples, surface ligands with electron-withdrawing fluorine groups were observed to increase the PSC performance.[20,22,29] Based on the data presented in these reports and the fact that these surface ligands should result in opposite trends in ELAs, variations in surface defect state passivation appear to be the dominant contributor to V_{OC} and PSC performance increases in these reports.

In reports where PSC improvements are ascribed to optimized ELAs, the ELA is typically inferred based on the ionization energies (valence band maxima/highest occupied molecular orbitals [HOMOs]) or electron affinities (conduction band minima/lowest unoccupied molecular orbitals [LUMOs]) measured on the isolated materials.[14,15,30,31] Such measurements fail to account for interfacial dipoles and band bending, thus reducing their direct translation to interfaces within the PSC. Reports that directly probe the ELA in the interfacial region rely on sequential deposition of the electron-transport layer (ETL) on the perovskite, which reveals a more complete picture of ELAs between the perovskite and the charge-transport layer.[32–37] However, these detailed studies of ELAs do not directly connect the ELAs to measurements of recombination dynamics. For example, transient absorption (TA) and transient reflectance (TR) spectroscopies are often used to investigate recombination dynamics in perovskites but have yet to be connected with detailed ELA measurements.[38–40] The same is true for device-level measurements of recombination dynamics, including transient photovoltage (TPV) and transient photocurrent (TPC).[41,42] Without such complementary measurements, it is difficult to understand the relationships between ligand structure, interfacial energetics, recombination dynamics, and PSC performance.

Here, we introduce three PEAI derivatives with different functional groups at the *para* position on the benzene ring, PEAI, 4-fluorophenethylammonium iodide (FPEAI), and 4-methoxyphenethylammonium iodide (MeOPEAI), at the interface between methylammonium lead iodide ($MAPbI_3$) and C_{60}. These ligands are selected to vary the interfacial energy landscape owing to the significant differences in the strength of the electron-donating or -withdrawing group in the *para* position. The enhancements of PSC performance depend on the surface ligand structure, with FPEAI showing the greatest V_{OC} and PCE. To examine the relationships between device performance, interfacial energetics, and charge-carrier recombination dynamics, we combine ultraviolet and inverse photoemission spectroscopy (UPS and IPES, respectively) measurements of interfacial energetics with TA, TR, TPV, and differential capacitance measurements to probe recombination dynamics. Using these complimentary techniques in combination allows us to disentangle how surface ligands inserted between the perovskite and the electron transport layer, C_{60}, impact recombination processes and device physics. The TR and TA measurements indicate that structural variations between these surface ligands have a minimal impact on recombination rates in bilayer films of $MAPbI_3$ and C_{60}; rather, UPS,

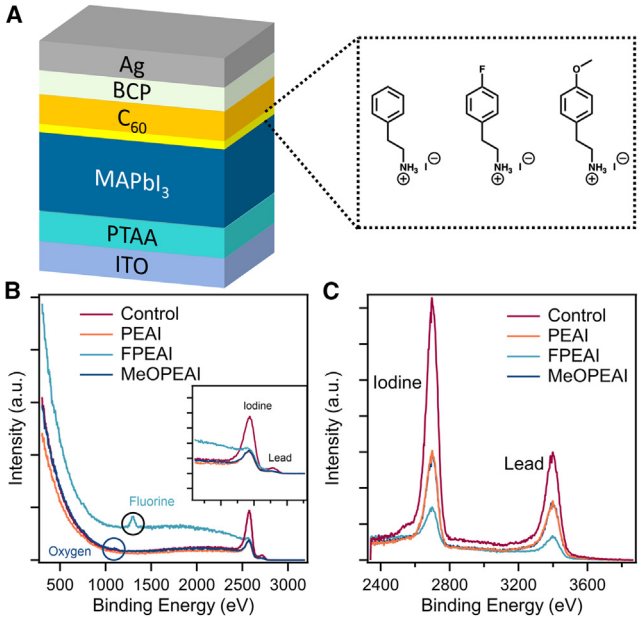

Figure 1. Surface ligand treatments on perovskite films and PSC devices

(A) Device structure of a p-i-n PSC with different surface ligands.

(B and C) Low-energy ion scattering spectra for the control and treated $MAPbI_3$ films collected with helium (B) and neon (C) ions.

TPV, and differential capacitance measurements indicate it is the increased interfacial energy gap that is responsible for the higher V_{OC} and improved PV performance observed with FPEAI modification.

RESULTS AND DISCUSSION

$MAPbI_3$ surface modification with PEAI derivatives

In this work, $MAPbI_3$ films were prepared using the previously reported one-step spin-coating method.[43] The surface modification was carried out by a post-film treatment method by casting an isopropanol solution (0.5 mg/mL) of PEAI, FPEAI, or MeOPEAI onto the thermally annealed $MAPbI_3$ films. Another 5 min thermal annealing process was further employed following ligand treatment. The whole process of $MAPbI_3$ film fabrication and treatment is illustrated in Figure S1. The inverted device architecture adopted in this work and the molecular structures of ligands are displayed in Figure 1A.

The impact of surface modification on the chemical and optoelectronic characteristics is partially related to the surface coverage of the ligands.[44] We firstly performed X-ray photoelectron spectroscopy (XPS) measurements to probe the elemental composition on the $MAPbI_3$ surface before and after surface treatments. The fluorine 1s peak at 687.85 eV and the oxygen 1s peak at 532.87 eV (Figure S2) indicate that FPEAI and MeOPEAI are anchored on the $MAPbI_3$ surface, respectively. The XPS data also show that PEAI is adsorbed on the surface, as the intensity of the carbon 1s signal from alkyl and aryl carbons at lower binding energies is increased relative to the methylammonium carbon at higher binding energies with PEAI treatment. The XPS spectral regions for nitrogen, lead, and iodine are displayed in Figure S2. Following surface ligand treatment, the XPS peaks for all elements shift slightly, which is attributed to changes in work function (WF) after surface treatment. Moreover, small Pb^0 peaks are found in all samples, with the FPEAI-treated sample

displaying the least amount of Pb^0. The presence of Pb^0 is attributed to excess PbI_2 on the surface degrading to Pb^0 under X-ray illumination.[45]

To further investigate the surface coverage with different ligands, we performed low-energy ion scattering spectroscopy (LEIS), which is only sensitive to the outermost atomic layer and thereby provides a more accurate probe of surface termination.[46] Here, helium ions (He^+) in LEIS (Figure 1B) were used to probe for oxygen and fluorine at energies of ~1,100 and ~1,300 eV, respectively. Neon ions (Ne^+) in LEIS were used to probe the surface composition of Pb and I. The spectra reveal that in all films, there is some amount of exposed Pb and I at the film surface, indicating incomplete ligand surface coverage (Figure 1C). As the surface coverage of the ligands is directly proportional to the signal intensity decrease of the covered elements,[46] we can easily quantify the surface coverage of each ligand by the reduced signal of the Pb peak (Figure S3). The fitted data are displayed in Table S1. Interestingly, though the three ligands are structurally identical near the ammonium binding group, FPEAI exhibits a higher surface coverage (83%) than PEAI (42%) and MeOPEAI (44%). We suspect that the higher surface coverage of FPEAI leads to the more stable $MAPbI_3$ surface under X-ray exposure.

To determine if the surface ligands altered the surface morphology of the $MAPbI_3$ films, top-view scanning electron microscopy (SEM) images were recorded. All films show similar morphologies, as displayed in Figure S4. The modified $MAPbI_3$ surfaces in Figure S4 show some small particles on smooth-textured crystalline grains, which are commonly found in low-dimensional capping layers.[47,48] We further probed for low-dimensional phases or other structural changes using X-ray diffraction (XRD; Figure S5), and no significant structural changes or low-dimensional phases are detected. The lack of observable XRD peaks from reduced dimensionality phases is attributed to the low ligand concentration (0.5 mg/mL) and short reaction time; however, these ligands can form 2D phases, and our results only indicate that 2D phase formation does not occur to an extent that can be detected with XRD. Increased ligand concentrations and increased reaction times were not pursued, as they decreased photovoltaic device performance.

Interfacial energetics at $MAPbI_3/C_{60}$ interfaces

The application of PEAI, FPEAI, or MeOPEAI results in a significant change of the surface electronic structure among the pristine and modified $MAPbI_3$ films, as probed by UPS and IPES. The energy levels presented in Figure 2A are shown with respect to the vacuum level (E_{vac} at 0 eV). The WF, valence band maximum (VBM; equated with the ionization energy), and conduction band minimum (CBM; equated with the electron affinity) are obtained from the UPS and IPES spectra, respectively (Figure 2B). Both the VBM and the CBM of the $MAPbI_3$ samples are determined using a Gaussian fit to the highest occupied and lowest unoccupied features in UPS and IPES spectra, as described in previous work and displayed in Figure S6.[34] This fitting procedure results in a VBM of 5.65 eV and a CBM of 4.11 eV for the pristine $MAPbI_3$ film with a WF of 4.93 eV. A large change in WF from 4.93 to 5.35 eV results from FPEAI treatment, which is attributed to the surface dipole introduced by FPEAI. The VBM and the CBM of FPEAI-modified $MAPbI_3$ increase to 5.95 and 4.24 eV, respectively. Only slight decreases in WF are found for both PEAI- (−0.05 eV) and MeOPEAI-modified (−0.07 eV) samples relative to the untreated $MAPbI_3$, and both the VBM and the CBM exhibit the same decreasing trend as the WF. The band gaps for all samples fall between 1.50 and 1.71 eV, with the MeOPEAI and FPEAI treatments resulting in the largest band gaps of 1.70 and 1.71 (±0.10) eV, respectively. These increases are at the edge of the uncertainty window and may be attributed to

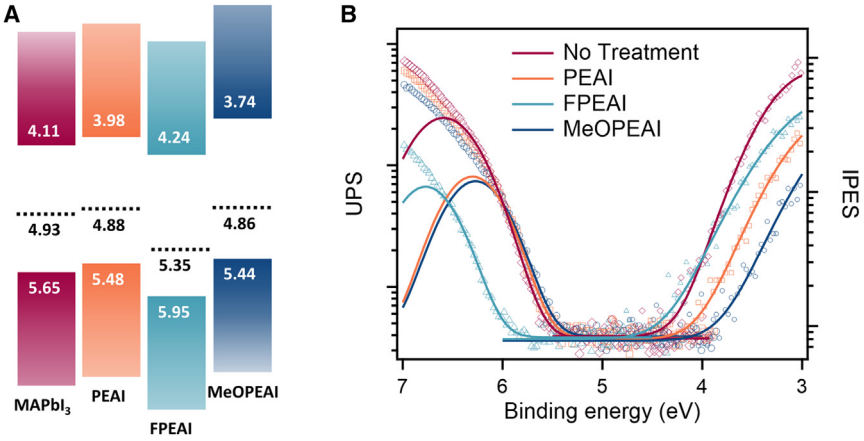

Figure 2. Surface energetics of perovskite films

(A) Energy levels for $MAPbI_3$ films with and without surface treatments.

(B) UPS and IPES spectra for $MAPbI_3$ films. Solid lines display Gaussian fits to the VBM and CBM onset regions.

differences in the extent of surface 2D phase formation, slight differences in surface chemistry, and/or differences in the electrostatic environment.

The modified $MAPbI_3$ energetics provide an important starting point for understanding interfacial energetics, but they do not capture effects such as band bending or interfacial dipoles introduced upon addition of the charge-transport layer. They also do not account for electrostatic induced shifts in the HOMO or LUMO of the organic semiconductor.[33,35] Therefore, we directly probed the interfacial energetics at the modified $MAPbI_3/C_{60}$ interface by *in situ* UPS measurements during incremental deposition of C_{60}.

Figure 3A shows the measured UPS spectra of the secondary electron cutoff (SECO) and the VBM/HOMO region as the thickness of C_{60} is increased from 0 to 256 Å on FPEAI-modified $MAPbI_3$. The measurements clearly show that the HOMO feature intensity of C_{60} gradually increases and the VB feature intensity of $MAPbI_3$ decreases as the C_{60} layer thickness increases. The SECO region shows that bare FPEAI-modified $MAPbI_3$ gives a WF of 5.35 eV, which decreases by 0.05 eV as the C_{60} thickness is increased to 256 Å. In contrast to the FPEAI-treated film, Figures 3B and 3C show dramatic increases in WF during C_{60} deposition for both PEAI- (0.29 eV) and MeOPEAI-modified (0.36 eV) $MAPbI_3$. The majority of the WF shift for PEAI- and MeOPEAI-modified $MAPbI_3$ occurs during the formation of a C_{60} bilayer (~16 Å), which is interpreted as an interfacial dipole. Herein, the interfacial dipole values shown in Figures 3E and 3F are taken as the WF difference between the modified perovskite film and the 16 Å C_{60}-coated film. Figure S7 shows the evolution of the UPS spectra in the VB/HOMO region for PEAI- and MeOPEAI-modified $MAPbI_3$ films as the C_{60} thickness is increased from 0 to 256 Å.

The UPS spectra were fit using a linear combination of the bare $MAPbI_3$ spectrum and the C_{60} spectrum at 256 Å thickness to extract the energy levels of both materials at varying C_{60} thicknesses, as illustrated in Figure S8. Combining all values extracted from the spectral fittings results in the energy diagrams presented in Figures 3D–3F. In addition to the differences in the WF changes observed with the different surface ligands, the energy diagrams show a slight upward bending of the C_{60} HOMO and LUMO near the interface with C_{60} for FPEAI and a slight

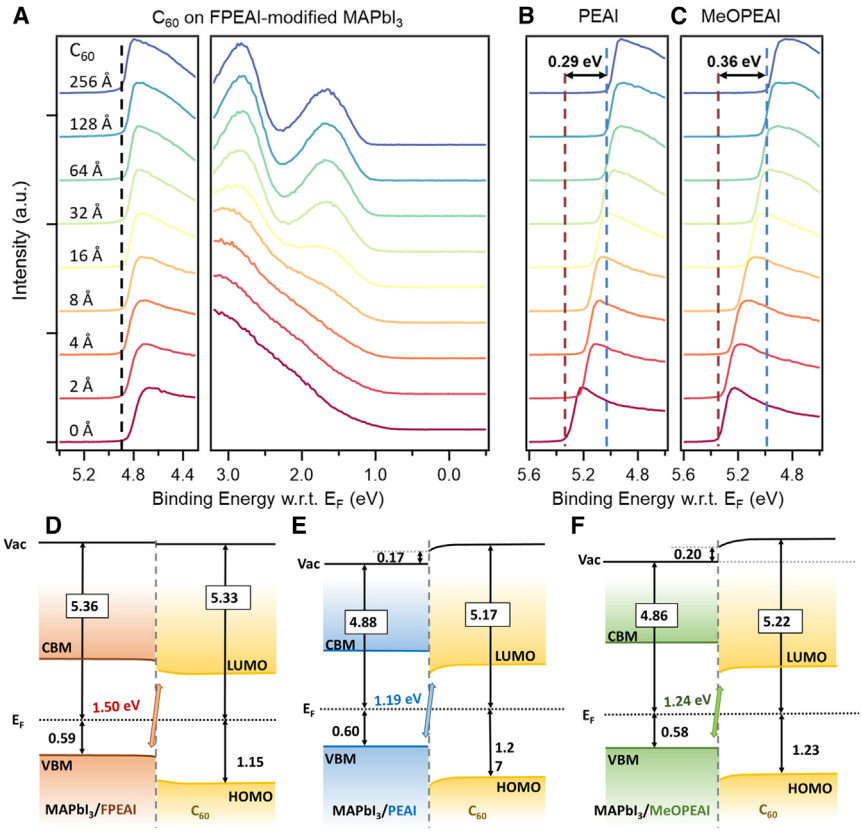

Figure 3. Interfacial energetics between modified perovskites and C_{60} layers

(A) UPS spectra of FPEAI-modified $MAPbI_3$ with stepwise deposition of C_{60} from 2 to 256 Å.

(B and C) SECO regions of UPS spectra for PEAI- (B) and MeOPEAI-modified (C) $MAPbI_3$ as the C_{60} thickness increases.

(D–F) Schematic diagrams of interfacial energetics between $MAPbI_3$ and C_{60} with FPEAI (D), PEAI (E), and MeOPEAI (F) treatments. The WF is calculated by the equation WF = $h\upsilon$(UPS) − SECO, where $h\upsilon$(UPS) is the energy of the excitation photons, 10.2 eV. All UPS spectra are presented with respect to (w.r.t.) the Fermi energy at 0 eV.

downward bending of the C_{60} HOMO and LUMO near the C_{60} interface for PEAI and MeOPEAI. These band-bending trends effectively increase the interfacial energy gap between the $MAPbI_3$ VBM and the C_{60} LUMO for FPEAI treatment and decrease this energy gap for PEAI and MeOPEAI treatments. The energy diagrams for the modified $MAPbI_3/C_{60}$ interfaces (Figures 3D–3F) show that the LUMOs of C_{60} lay lower in energy than the CBMs of $MAPbI_3$ by 0.31, 0.21, and 0.46 eV for PEAI-, FPEAI-, and MeOPEAI-modified interfaces, respectively, as determined at 16 Å of C_{60}. The HOMO of C_{60} is also lower than the VBM of $MAPbI_3$, thus forming a type 2 heterojunction that favors electron transfer and hinders hole transfer from $MAPbI_3$ to C_{60}.

Nonoptimal ELAs at interfaces in PSCs can result in a smaller interfacial energy gap, leading to a dramatic bending of the quasi-Fermi level close to the interface, as determined by simulations, and consequently a V_{OC} loss.[18,49,50] In an ideal photovoltaic cell, the V_{OC} limit is directly related to the optical gap of the absorber; however, the interfacial energy gaps at the absorber/charge-transport layer (CTL) interfaces can limit the V_{OC} if they are smaller than the optical gap of the material.[18] The interfacial energy gaps between the $MAPbI_3$ VBM and the C_{60} LUMO at the

Table 1. Photovoltaic performance of the control device and the surface-modified devices

		J_{SC} (mA·cm^{-2})	VOC (V)	FF	PCE (%)
Control	RS	22.47 ± 0.26 (22.82)	1.03 ± 0.01 (1.03)	0.778 ± 0.009 (0.787)	18.0 ± 0.4 (18.5)
	FS	22.37 ± 0.22 (22.80)	1.02 ± 0.01 (1.03)	0.761 ± 0.012 (0.752)	17.3 ± 0.11 (17.6)
With PEAI	RS	22.19 ± 0.12 (22.34)	1.07 ± 0.01 (1.07)	0.790 ± 0.014 (0.797)	18.7 ± 0.3 (19.0)
	FS	22.20 ± 0.11 (22.34)	1.07 ± 0.01 (1.06)	0.759 ± 0.013 (0.776)	18.0 ± 0.3 (18.4)
With FPEAI	RS	22.05 ± 0.11 (22.17)	1.10 ± 0.01 (1.11)	0.811 ± 0.006 (0.814)	19.6 ± 0.2 (20.0)
	FS	22.01 ± 0.14 (22.08)	1.09 ± 0.01 (1.10)	0.797 ± 0.006 (0.798)	19.2 ± 0.2 (19.3)
With MeOPEAI	RS	22.13 ± 0.14 (22.18)	1.07 ± 0.01 (1.07)	0.800 ± 0.013 (0.813)	18.9 ± 0.3 (19.3)
	FS	22.13 ± 0.15 (22.17)	1.07 ± 0.01 (1.07)	0.782 ± 0.011 (0.789)	18.4 ± 0.3 (18.7)

Champion device parameters are shown in parentheses.

$MAPbI_3/C_{60}$ interfaces can be determined from the stepwise UPS measurements (using the UPS-/IPES-determined band gap of pure C_{60} to estimate the LUMO) at small C_{60} thicknesses, where both the $MAPbI_3$ VBM and the C_{60} HOMO energy can be extracted. Here, at a C_{60} thickness of 16 Å, the FPEAI-modified sample exhibits a greater interfacial energy gap (i.e., the difference between the $MAPbI_3$ VBM and the C_{60} LUMO) of 1.50 eV, as compared to only 1.19 and 1.24 eV for the PEAI- and MeOPEAI-modified samples, respectively. The interfacial energy gaps of 1.19 and 1.24 eV for PEA- and MeOPEAI-modified interfaces are significantly lower than the band gap of $MAPbI_3$ and thus may limit the QFLS in the PSC device.[18]

Enhanced photovoltaic performance of PSCs by surface modification

To investigate the impact of surface modification on photovoltaic performance, we fabricated planar PSCs with an inverted architecture of indium tin oxide (ITO)/poly[bis(4-phenyl)(2,4,6-trimethylphenyl)amine (PTAA)/PFN-Br/$MAPbI_3$/surface ligand/C_{60}/bathocuproine (BCP)/Ag. Herein, the poly[(9,9-bis(3′-((N,N-dimethyl)-N-ethyl-ammonium)-propyl)-2,7-fluorene)-alt-2,7-(9,9-dioctylfluorene)]-dibromide (PFN-Br) thin layer was spun cast on PTAA to enhance the wettability of the $MAPbI_3$ precursor solution, leading to dense and pinhole-free $MAPbI_3$ films. The device efficiencies increase to varying extents with the different surface ligands, as displayed in Table 1. The champion PCE is obtained in an FPEAI-modified device, achieving a reverse-scanned (RS) PCE of 20.0% with a V_{OC} of 1.11 V, a short-circuit current density (J_{SC}) of 22.17 mA/cm^2, and a fill factor (FF) of 0.814 (Figure 4A), with a small hysteresis index (HI) of 3.74%. The HI is calculated via Equation S1. In contrast, the best control device delivered an RS PCE of 18.5%, with a V_{OC} of 1.03 V, a J_{SC} of 22.82 mA/cm^2, an FF of 0.787, and an HI of 6.42%. The best RS PCEs from PEAI- and MeOPEAI-modified devices are 19.0% and 19.3%, respectively. In addition, steady-state power output of the champion cell shows a stabilized PCE of 19.7% from the FPEAI-modified device, agreeing with the average of RS and forward-scanned (FS) PCEs (Figure 4B). The device J_{SC} experiences a slight decrease after all surface ligand treatments, which is verified by the distinguishable drop in the external quantum efficiency (EQE) for all three modified devices in comparison with that of the control devices (Figure 4C). A box and whisker plot of device V_{OC} and PCE from 20 cells for each surface ligand and the control are displayed in Figure 4D.

Charge-carrier behavior at $MAPbI_3/C_{60}$ interfaces

Steady-state and transient optical measurements are applied to investigate the impact of surface ligands on charge-carrier recombination. Photoluminescence (PL) spectra were collected on ligand-treated $MAPbI_3$ with and without C_{60}. As shown in Figure S9, the PL peaks are centered at 770 nm for all samples. For surface-treated $MAPbI_3$ films without C_{60}, PEAI and MeOPEAI enhance the PL intensity,

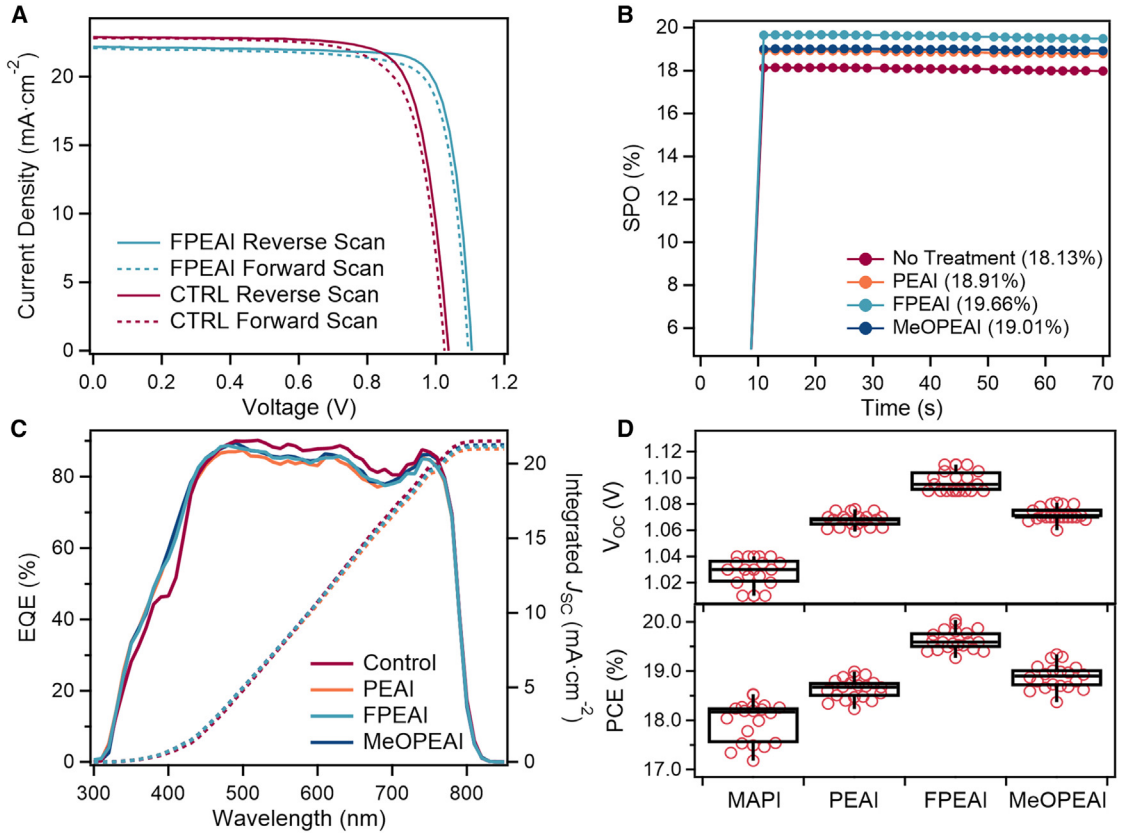

Figure 4. Performance of PSC devices

(A) J-V characteristics of champion devices for FPEAI modification and with no surface ligand treatment (control).

(B) Stabilized power outputs (SPOs).

(C) External quantum efficiency (EQE) spectra and the corresponding integrated short-circuit current density (J_{SC}).

(D) Box and whisker plot of the open-circuit voltage (V_{OC}) and power conversion efficiency (PCE). Red circles represent individual photovoltaic cells.

while the intensity with FPEAI treatment is similar to unmodified $MAPbI_3$. When a 30-nm-thick layer of C_{60} is present, the differences between the films are greatly enhanced. Here, all ligands increase the PL intensity by at least a factor of six relative to the untreated bilayer, with the FPEAI-treated $MAPbI_3/C_{60}$ bilayer showing the highest PL intensity, which is approximately 20 times more intense than the untreated sample. These intensity enhancements with ligand treatment are attributed to reduced interfacial recombination relative to the untreated $MAPbI_3/C_{60}$ bilayer.

To further investigate the charge transfer and recombination dynamics at the interface between $MAPbI_3$ and C60, we employed TA and TR on the $MAPbI_3/C_{60}$ bilayers, as illustrated in Figure 5A. In these measurements $MAPbI_3$ is directly deposited on glass substrates. Firstly, TA was performed on the modified $MAPbI_3$ to investigate the impact of ligands on charge recombination dynamics throughout the whole $MAPbI_3$ film (Figure S10). The spectral range considered spans from 550 to 850 nm, with the negative change in optical density (ΔOD) centered at 758 nm representing the ground-state bleach (GSB) of $MAPbI_3$. In the normalized TA kinetic profiles (Figure S11), the control and modified films display nearly identical decay dynamics over the 2.5 ns probing range among 4 different films. As TA probes the full film thickness, the influence from the thin modified layers may be overshadowed by the dynamics in the bulk.[38,39] To determine how the surface ligands impact

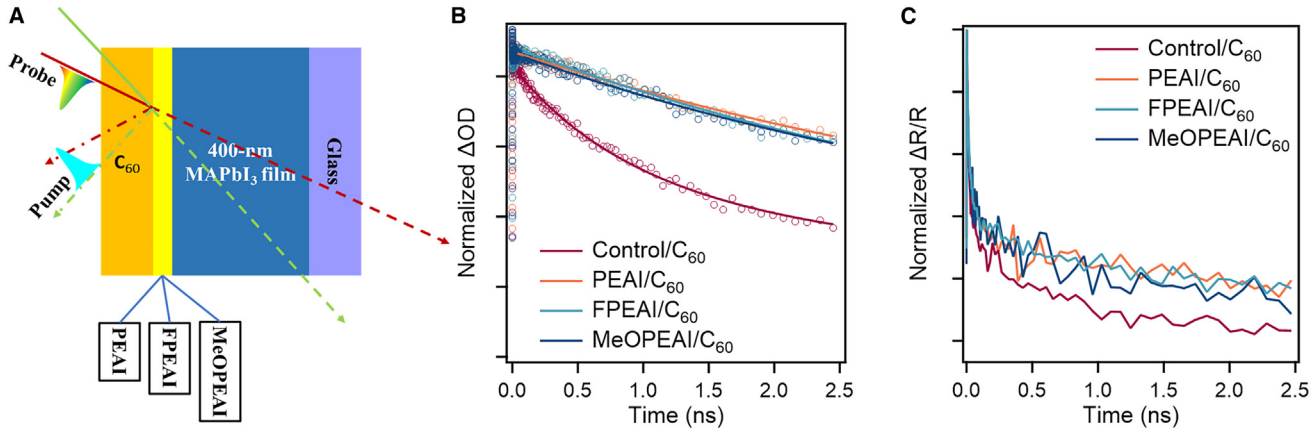

Figure 5. TA and TR spectra of the $MAPbI_3/C_{60}$ bilayer films

(A) Schematics of TA and TR spectroscopies on $MAPbI_3/C_{60}$ samples.

(B) TA kinetics for C_{60}-coated $MAPbI_3$ films with and without surface ligands.

(C) TR kinetics for C_{60}-coated $MAPbI_3$ films with and without surface ligands.

recombination dynamics at the interface with C_{60}, 25 nm C_{60} was thermally evaporated onto the pristine and modified $MAPbI_3$ films. The TA decay curves displayed in Figure S12 show that the deposition of C_{60} on pristine $MAPbI_3$ accelerates the decay of the GSB in $MAPbI_3$, which can be attributed to electron transfer from $MAPbI_3$ to C_{60}.[51,52] Further comparison was carried out among C_{60}-coated $MAPbI_3$ films with different surface ligands, as shown in Figures 5B and S13. No peak shift or shape change was noticed for the GSB, which remains centered at 758 nm for the ligand-treated films. Spectra in the first 2.5 ns indicate similar decay dynamics for all ligand-treated films and show that ligand treatment increases the excited-state lifetime. The longer excited-state lifetime for all ligand-modified $MAPbI_3/C_{60}$ bilayers indicates that the surface ligands decrease the charge recombination rate, which agrees with the increase in V_{OC} for the ligand-treated PSCs. We attribute this ligand-independent increase in lifetime to the suppression of interfacial defects. Interestingly, even though the V_{OC} is 0.02–0.04 V larger for FPEAI-treated $MAPbI_3$ compared with PEAI- or MeOPEAI-treated $MAPbI_3$, all ligand-treated films show nearly identical recombination dynamics via TA analysis. Here, excited-state lifetimes of 5.43 $\pm$ 0.36 ns are observed for the ligand-treated films, while a lifetime of only 1.15 ns is observed for the control. The fitting results are displayed in Table S2.

TA is useful for understanding the bulk excited-state properties of materials since the probe beam directly passes through the entire material. However, TR is a surface-sensitive technique where only the first tens of nanometers are optically excited and probed. Therefore, we conducted TR measurements to isolate the effects of the ligand treatments. The TR measurements were conducted by monitoring the pump-induced changes of the reflection ($\Delta R/R$) from the front surface, corresponding to the real part, *n*, dominating the refractive index near the band edge of semiconductors.[38–40] TR measurements were performed using the same C_{60}-coated films as used for TA (Figure 5C). By the inherent relation between steady-state absorption and reflection, we convert as-measured TR to TA spectra using the Kramer-Kronig (K-K) transformation, as shown in Figure S14.[38] By comparing the K-K transform of TA and experimental TR, the 400-nm-thick $MAPbI_3$ films appear free of thin-film interference effects in the spectral range of interest.[39] From the normalized TR results representing the decay kinetics (Figure 5C),

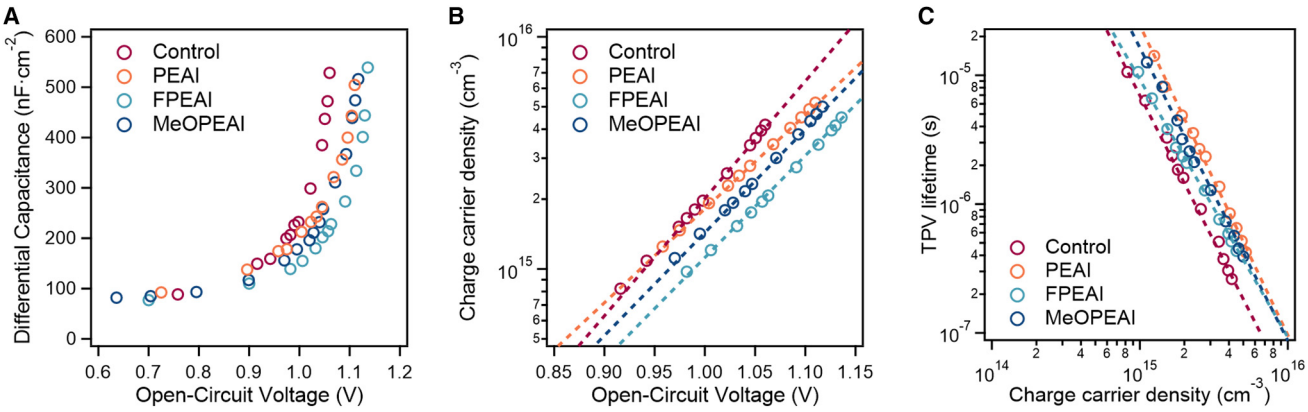

Figure 6. Transient photovoltage and photocurrent analysis

(A) Differential capacitance as a function of V_{OC}.

(B) Charge-carrier density in the devices as a function of V_{OC}.

(C) TPV charge-carrier lifetime vs. charge-carrier density for devices with and without surface ligands.

the ligand-treated films exhibit longer-lived GSB signals within 2.5 ns as probed at 760 nm than the nontreated $MAPbI_3$ films, indicating that charge-carrier recombination rates are reduced upon ligand treatment. However, like the TA results, the overall excited-state TR lifetime is independent of the ligand used. These data thus lead us to question the origin for the V_{OC} enhancement from the FPEAI treatment relative to PEAI and MeOPEAI.

TPV/TPC and differential capacitance analysis of PSC devices

TA and TR show that recombination differences in the bilayer films cannot explain the V_{OC} differences. Thereby, we turn to TPV and TPC measurements on complete devices to better understand recombination dynamics in PSCs and the origin of the V_{OC} change. A combination of TPV and TPC measurements enables the differential capacitance to be extracted.[41,42,53] Briefly, a small perturbation from a laser pulse is applied to a device under illumination from a steady-state light source, with the V_{OC} held at different values through varying the steady-state light source intensity. A range of light intensities from 0.01 to 1 sun equivalency were employed during the measurements. The excess charge carriers generated by the laser pulse then recombine at open circuit in TPV or are collected at short circuit in TPC. The excess charges (Δq) can be calculated by the integration of the TPC response. The differential capacitance is calculated as

$$dC(V) = \frac{\Delta q}{\Delta V(V_{OC})} \qquad \text{(Equation 1)}$$

where $\Delta V(V_{OC})$ is the amplitude of the TPV transient measured at various V_{OC}, corresponding to different background light intensities. Typically, Δq is independent of background light when measured at a lower light intensity, suggesting that the recombination process is negligible at short circuit. As illustrated in Figure 6A, without any background light, dC(0), reflecting the electrode capacitance ($C_{electrode}$), is similar for all devices at around 80 nF/cm^2. The electrode capacitance, where charge carriers are accumulated at the ITO and Ag contacts, appears independent of light bias under low background light illumination.[41,54] As the background light intensity increases, dC exponentially increases with respect to V_{OC}. This capacitance can be assigned to the $MAPbI_3$ active layer and the interface regions between $MAPbI_3$ and charge-transporting layers.[41] The total excess areal

charge density (Q) stored in the device at open circuit can be estimated by integrating dC over V_{OC} via Equation 2.

$$Q = \int_0^{V_{OC}} dC(V) - C_{electrode} dV \quad \text{(Equation 2)}$$

where $\Delta V(V_{OC})$ is the amplitude of the TPV transient measured at various V_{OC}, corresponding to different background light intensities. Typically, Δq is independent of background light when measured at a lower light intensity, suggesting that the recombination process is negligible at short circuit. As illustrated in Figure 6A, without any background light, dC(0), reflecting the electrode capacitance ($C_{electrode}$), is similar for all devices at around 80 nF/cm^2. The electrode capacitance, where charge carriers are accumulated at the ITO and Ag contacts, appears independent of light bias under low background light illumination.[41,54] As the background light intensity increases, dC exponentially increases with respect to V_{OC}. This capacitance can be assigned to the $MAPbI_3$ active layer and the interface regions between $MAPbI_3$ and charge-transporting layers.[41] The total excess areal charge density (Q) stored in the device at open circuit can be estimated by integrating dC over V_{OC} via Equation 2.

Figure S15 plots Q as a function of V_{OC}, and the charge-carrier density can be derived by Equation S1. Figure 6A shows that the differential capacitance curve shifts to the right (to higher voltages) for all surface-ligand-modified PSCs, with the FPEAI-modified sample showing the greatest shift. Correspondingly, Figure 6B shows that for a similar charge-carrier density FPEAI will show the highest V_{OC} and the unmodified film the lowest V_{OC}. Such results agree with the UPS measurements, where the energy gap at the $MAPbI_3/C_{60}$ interface is greatest for FPEAI-treated $MAPbI_3$. This combination of results indicate that it is the interfacial energetics that are dominating the V_{OC} changes based on ligand structure and not variations in defect states or interfacial electronic coupling.

We further investigated the corresponding charge-carrier lifetime with respect to charge-carrier density as displayed in Figure 6C. The lifetimes are extracted from TPV transients, indicating the charge recombination rate. All TPV transients decay monoexponentially as presented in Figure S16. An approximate power-law correlation was observed for all devices as expected for a bimolecular charge recombination process.[55] Under 1 sun equivalent light irradiation, the three modified PSCs exhibited similar recombination rates with TPV transient lifetimes of 424 ns for PEAI-, 433 ns for FPEAI-, and 392 ns for MeOPEAI modified devices, while the TPV transient decayed with a lifetime of 262 ns for the control device (Figure S17). Figure S18 shows the light intensity dependence of V_{OC}, which allows the identification of the ideality factor, n_{id}, by Equation S2. Comparable ideality factors indicate similar recombination processes with and without surface ligands,[56] which further supports that interfacial energetic differences are the primary variable influencing the V_{OC}, as opposed to differences in interfacial defect states.

In this article, the TA and TR results presented show that all ammonium ligands investigated here increase the recombination lifetime in $MAPbI_3/C_{60}$ bilayers; however, the TA- and TR-determined lifetimes do not depend on surface ligand structure, as all three ligand-treated interfaces show nearly identical recombination dynamics. Similarly, TPV measurements of the PSCs show increased recombination lifetimes upon ligand treatment but minimal differences between the different surface ligands at comparable charge-carrier densities. This information shows that ligand treatment can reduce recombination and boost solar cell performance just through

surface passivation and that the variations in ligand structure investigated here exert only minimal differences in recombination dynamics when these dynamics are compared at similar charge-carrier densities. Understanding the PSC performance variations between the different surface ligands requires consideration of the UPS and differential capacitance results, which show that the V_{OC} varies in accordance with the energy gap at the $MAPbI_3/C_{60}$ interface. Our work suggests that, while ligand treatments passivate the interface between perovskites and charge-transport layers, variations in interfacial energetics can be a major contributor to performance variations observed upon surface ligand treatment of PSCs.

This work also highlights that the application of multiple transient methods, including those performed on complete devices, is often necessary to understand the device physics that leads to performance variations in PSCs. For example, surface ligand modification may improve device performance through shifting the interfacial energetics, as demonstrated here, while there may be other systems where surface ligands have minimal effect on energetics and instead alter the recombination dynamics at comparable charge-carrier densities to shift the V_{OC}. From a surface ligand design standpoint, adjusting the dipole moment of the surface ligand provides a straightforward way to manipulate the interfacial energy gap and increase the V_{OC}. Many questions related to surface ligands still remain, including how both the extent of surface coverage and 2D phase formation impact recombination dynamics. Moving forward, after the energetic alignment is optimized in a particular system, further gains in V_{OC} and PCE could be achieved through more effective defect state passivation or reduced interfacial electronic coupling to further reduce the interfacial recombination rates.

EXPERIMENTAL PROCEDURES

Resource availability

Lead contact

Further information and requests for the resources are available from the lead contact, Kenneth R. Graham (kenneth.graham@uky.edu).

Materials availability

This study did not generate new unique materials.

Data and code availability

All data during this study can be accessed in the article and its supplemental information.

Materials

All reagents were directly used without further purification. Methylammonium iodide (MAI), PEAI, FPEAI, and MeOPEAI were purchased from Greatcell Solar Materials. PTAA was obtained from Solaris Chem. C_{60} was purchased from Lumtec. PFN-Br was acquired from 1-Material. BCP and all solvents, including *N,N*-dimethylformamide (DMF), dimethyl sulfoxide (DMSO), methanol (MeOH), toluene, and isopropanol (IPA) were from Sigma-Aldrich.

Film and device fabrication

ITO-coated glass substrates (15 Ω/□) were cleaned with sodium dodecyl sulfate solution, water, acetone, and IPA sequentially and then treated with UV-ozone for 15 min before film fabrication. The PTAA layer was spin-coated onto the ITO substrates (2 mg/mL in toluene) at 6,000 rpm for 30s and annealed at 100°C for 10 min. The $MAPbI_3$ precursor solution was prepared by dissolving 238.5 mg MAI

and 726.1 mg PbI_2 in 1 mL DMF/DMSO mixed solvent (v/v 9/1). PFN-Br was dissolved in MeOH at 0.5 mg/mL. The thin PFN-Br layer was deposited on PTAA by spin-coating at 4,000 rpm for 30 s to enhance the wettability of the $MAPbI_3$ precursor solution. The $MAPbI_3$ layer was fabricated by spin-coating 150 μL $MAPbI_3$ precursor solution at a speed of 4,000 rpm for 30 s. During spinning, 200 μL toluene was dropped onto the film at the 10th second following the start of spinning. The as-cast films were further annealed at 100°C for 10 min. For surface modifications, all ligands were dissolved in IPA at 0.5 mg/mL. The surface ligand solutions were spun cast on $MAPbI_3$ films at 3,000 rpm for 30 s, followed by a 5 min annealing process at 100°C. Finally, 25 nm C_{60}, 6 nm BCP, and 100 nm Ag were deposited through thermal evaporation. The device active area by evaporation was 0.122 cm^2, which was masked during the J-V measurement with a 0.059 cm^2 metal aperture mask. $MAPbI_3$ films for TA and TR measurements were fabricated on glass substrates under the same conditions.

Device characterizations

The J-V curves were recorded with a scan rate of 0.34 V s^{-1} in an N_2-filled glovebox under light illumination from a Newport Oriel Sol3S class solar simulator with a xenon lamp, calibrated with a silicon cell under a KG2 filter before measurements. The stabilized power outputs (SPOs) of the devices were measured by monitoring the current density output under a bias potential set at the maximum power point. EQE spectra were obtained in ambient air using a Newport Oriel IQE200 system with monochromatic light scanning from 300 to 800 nm.

UPS and IPES measurements

Photoemission spectroscopy measurements were carried out in a PHI 5600 ultrahigh vacuum (UHV) system under a base vacuum of 5×10^{-10} mbar. All as-prepared $MAPbI_3$ films were transferred into the UHV chamber without air exposure through a glovebox under N_2 atmosphere. UPS measurements were conducted with an 11-inch-diameter hemispherical electron energy analyzer and multichannel detector with a pass energy of 5.85 eV. Photons with energies of 10.2 eV, as produced by an Excitech H Lyman-α lamp (E-LUX 121), were used as the excitation source. A −5 V bias was employed in all UPS measurements. IPES measurements were performed in the same UHV chamber. During the data collection, the chamber was blacked out to eliminate external photons. IPES spectra were obtained in the isochromat mode with a 254 nm optical band-pass filter coupled to a photomultiplier tube. The low-energy electron beam was generated by a Kimball Physics ELG-2 electron gun equipped with a BaO cathode. To minimize sample damage, electron kinetic energies were kept at <5 eV after −20 V bias deceleration, and emission currents were set at 2 μA. Samples for PES measurements were prepared on nonpatterned ITO substrates with the PTAA hole-transporting layer (HTL) and PFN-Br layers. During the incremental depositions of C_{60}, the rate was maintained at <0.5 Å/s and the pressure at $<5 \times 10^{-7}$ mbar, with the samples kept under vacuum between measurements.

PL

PL spectra of thin films were acquired by an Ocean Optics QE Pro high-performance spectrometer under 532 nm laser (Thorlabs, CPS532) irradiation with 1,100 ms integration time and 200 μm slit width.

TA measurement

TA measurements were collected using a PHAROS Yb:KGW laser with an output of 1,028 nm at 1 kHz. The laser beam was directed into an ORPHEUS optical parametric amplifier to generate a pump laser pulse (<190 fs), modulated at 500 Hz through an

optical chopper. Femtosecond TA spectra were probed up to 7 ns by a Helios system (Ultrafast Systems) with a visible white light continuum generated by a sapphire crystal.

TR measurement

TR measurements were conducted with a Coherent laser (800 nm fundamental beam, 1 kHz repetition rate, 3 mJ pulse, and 100 fs pulse width). The laser beam was split into pump and probe pulses. The pump laser pulse was directed into a Palitra Duo optical parametric amplifier to obtain a 400 nm pump laser. The probe was directed through a sapphire crystal to generate a white light continuum with a delay of up to 2.5 ns. The pump and probe pulses were aligned spatially at an approximately 45° angle to the sample surface. A Helios ultrafast spectrometer was employed to collect TR signals with a 90° angle to the probe and pump beams. The excitation density for all TR measurements was kept the same at 6×10^{13} photons•cm^{-2}. Films for TR measurements are the same as for TA measurements.

TPV/TPC measurement

TPV/TPC measurements were carried out in a home-built system. Background white light illumination with variable intensity was provided by a LUXEON SP-12-W5 LED module, consisting of a cool white Rebel LED on a SinkPAD-II square base and a 9° optic. An extra convex lens is located between the LED and the PSC to concentrate the light onto the active area of the devices. By controlling the working voltage for the LED module, the light intensity on the device can reach up to 2 sun intensity equivalence. A Thorlabs L520P50 laser diode, exciting at 520 nm, was chosen as the source of the laser pulse perturbation. Both the white light LED and the green laser diode are powered and controlled by an arbitrary waveform generator, Keysight 33522B. Normally, to obtain a distinguishable TPV signal at high light intensity, the pulse was set with a width of 200 ns and an 8.4 ns pulse edge and was repeated every second (1 Hz). All TPV and TPC transients were probed via a Tektronix MDO3024 oscilloscope in trigger mode.

LEIS

The LEIS technique was used to study the coverage of surface ligands on perovskite films. LEIS measurements were performed using an IONTOF Qtac100 tool under a base vacuum of 1×10^{-10} mbar. He^+ and Ne^+ ion guns were installed for LEIS measurement at a normal incidence angle. The He^+ ion beam was generated at 3 keV kinetic energy with 3 nA ion current, and the Ne^+ ion beam was generated with 3 keV kinetic energy and 5 nA current. All samples were transferred into the system with limited air exposure. No sputtering or cleaning processes were conducted before measurements. The He^+ ion source was used to measure the low-atomic mass elements, including O and F, and an Ne^+ ion source was used to measure Pb and I.

XRD measurement

XRD was performed to assess the crystal structures of $MAPbI_3$ films using a Rigaku D-Max 2200 X-ray diffractometer.

SEM measurements

SEM was used to characterize the morphology and microstructure change of the $MAPbI_3$ films using a Hitachi S-4800 scanning electron microscope.

SUPPLEMENTAL INFORMATION

Supplemental information can be found online at https://doi.org/10.1016/j.xcrp.2023.101650.

ACKNOWLEDGMENTS

We acknowledge Thomas Heumüller for sharing helpful design details relevant to the development of our TPV and TPC setup. T.L. and K.R.G. acknowledge funding from the National Science Foundation under award OIA-1929131. T.L., H.R.A., H.P., and K.R.G. acknowledge funding from the US Department of Energy (DOE), Office of Basic Energy Sciences, under grant DE-SC0018208 for supporting the photoemission spectroscopy measurements and TPV and TPC measurements. S.J. and K.R.G. acknowledge support from the National Science Foundation under cooperative agreement no. 1849213. The LEIS measurements were enabled by National Science Foundation MRI #1919845 and performed at Colorado Shared Instrumentation in Nanofabrication and Characterization (COSINC) at the University of Colorado, Boulder. Work at NREL was supported through the Center for Hybrid Organic Inorganic Semiconductors for Energy (CHOISE), an Energy Frontier Research Center funded by the Office of Basic Energy Sciences, Office of Sciences, within the DOE. The views expressed in the article do not necessarily represent the views of the DOE or the US government.

AUTHOR CONTRIBUTIONS

T.L. performed PSC device fabrication and film and device characterization, designed and carried out TPV measurements, and prepared the manuscript. R.A.S. performed TR and TA measurements. X.Z. and M.C. helped improve the PSC device fabrications. T.L. and S.J. measured *in situ* UPS and IPES. Q.J. conducted XRD and SEM measurements. H.R.A. carried out the XPS measurements. H.P. helped with ligand preparation. K.Z. and J.M.L. contributed to the analysis and provided advice. M.C.B. and K.R.G. supervised the study, and K.R.G. helped write the manuscript. M.C.B., K.R.G., and R.A.S. helped revise the manuscript. The manuscript reflects the contributions of all authors.

DECLARATION OF INTERESTS

The authors declare no competing interests.

INCLUSION AND DIVERSITY

We support inclusive, diverse, and equitable conduct of research.

Received: July 28, 2023
Revised: September 13, 2023
Accepted: September 28, 2023
Published: October 18, 2023

REFERENCES

1. Kojima, A., Teshima, K., Shirai, Y., and Miyasaka, T. (2009). Organometal Halide Perovskites as Visible-Light Sensitizers for Photovoltaic Cells. J. Am. Chem. Soc. *131*, 6050–6051. https://doi.org/10.1021/ja809598r.

2. Kim, H.-S., Lee, C.-R., Im, J.-H., Lee, K.-B., Moehl, T., Marchioro, A., Moon, S.-J., Humphry-Baker, R., Yum, J.-H., Moser, J.E., et al. (2012). Lead Iodide Perovskite Sensitized All-Solid-State Submicron Thin Film Mesoscopic Solar Cell with Efficiency Exceeding 9%. Sci. Rep. *2*, 591. https://doi.org/10.1038/srep00591.

3. Lee, M.M., Teuscher, J., Miyasaka, T., Murakami, T.N., and Snaith, H.J. (2012). Efficient Hybrid Solar Cells Based on Meso-Superstructured Organometal Halide Perovskites. Science *338*, 643–647. https://doi.org/10.1126/science.1228604.

4. Jeon, N.J., Noh, J.H., Yang, W.S., Kim, Y.C., Ryu, S., Seo, J., and Seok, S.I. (2015). Compositional engineering of perovskite materials for high-performance solar cells. Nature *517*, 476–480. https://doi.org/10.1038/nature14133.

5. Zheng, X., Chen, B., Dai, J., Fang, Y., Bai, Y., Lin, Y., Wei, H., Zeng, X., and Huang, J. (2017). Defect passivation in hybrid perovskite solar cells using quaternary ammonium halide anions and cations. Nat. Energy *2*, 17102. https://doi.org/10.1038/nenergy.2017.102.

6. Jiang, Q., Zhao, Y., Zhang, X., Yang, X., Chen, Y., Chu, Z., Ye, Q., Li, X., Yin, Z., and You, J. (2019). Surface passivation of perovskite film for efficient solar cells. Nat. Photonics *13*, 460–466. https://doi.org/10.1038/s41566-019-0398-2.

7. Min, H., Lee, D.Y., Kim, J., Kim, G., Lee, K.S., Kim, J., Paik, M.J., Kim, Y.K., Kim, K.S., Kim, M.G., et al. (2021). Perovskite solar cells with atomically coherent interlayers on SnO2 electrodes. Nature *598*, 444–450. https://doi.org/10.1038/s41586-021-03964-8.

8. National Renewable Energy Laboratory (2023). Best Research-Cell Efficiencies. https://www.nrel.gov/pv/assets/pdfs/best-research-cell-efficiencies.pdf.

9. Zhang, J., Zhang, W., Cheng, H.-M., and Silva, S.R.P. (2020). Critical review of recent progress of flexible perovskite solar cells. Mater. Today *39*, 66–88. https://doi.org/10.1016/j.mattod.2020.05.002.

10. Kim, D.H., Muzzillo, C.P., Tong, J., Palmstrom, A.F., Larson, B.W., Choi, C., Harvey, S.P., Glynn, S., Whitaker, J.B., Zhang, F., et al. (2019). Bimolecular Additives Improve Wide-Band-Gap Perovskites for Efficient Tandem Solar Cells with CIGS. Joule *3*, 1734–1745. https://doi.org/10.1016/j.joule.2019.04.012.

11. Zheng, X., Liu, J., Liu, T., Aydin, E., Chen, M., Yan, W., De Bastiani, M., Allen, T.G., Yuan, S., Kirmani, A.R., et al. (2022). Photoactivated p-Doping of Organic Interlayer Enables Efficient Perovskite/Silicon Tandem Solar Cells. ACS Energy Lett. *7*, 1987–1993. https://doi.org/10.1021/acsenergylett.2c00780.

12. Jiang, Y., He, S., Qiu, L., Zhao, Y., and Qi, Y. (2022). Perovskite solar cells by vapor deposition based and assisted methods. Appl. Phys. Rev. *9*, 021305. https://doi.org/10.1063/5.0085221.

13. Jiang, Q., Tong, J., Xian, Y., Kerner, R.A., Dunfield, S.P., Xiao, C., Scheidt, R.A., Kuciauskas, D., Wang, X., Hautzinger, M.P., et al. (2022). Surface reaction for efficient and stable inverted perovskite solar cells. Nature *611*, 278–283. https://doi.org/10.1038/s41586-022-05268-x.

14. Jiang, X., Wang, F., Wei, Q., Li, H., Shang, Y., Zhou, W., Wang, C., Cheng, P., Chen, Q., Chen, L., and Ning, Z. (2020). Ultra-high open-circuit voltage of tin perovskite solar cells via an electron transporting layer design. Nat. Commun. *11*, 1245. https://doi.org/10.1038/s41467-020-15078-2.

15. Chen, H., Li, Q., You, S., Huang, X., Fan, C., Lin, Z., Qiu, B., Park, S.M., Atapattu, H.R., Gao, Y., et al. (2022). Quantum-size-tuned heterostructures enable efficient and stable inverted perovskite solar cells. Mikrochim. Acta *189*, 352–358. https://doi.org/10.1038/s41566-022-00985-1.

16. Zhao, T., Chueh, C.-C., Chen, Q., Rajagopal, A., and Jen, A.K.Y. (2016). Defect Passivation of Organic–Inorganic Hybrid Perovskites by Diammonium Iodide toward High-Performance Photovoltaic Devices. ACS Energy Lett. *1*, 757–763. https://doi.org/10.1021/acsenergylett.6b00327.

17. Li, F., Deng, X., Qi, F., Li, Z., Liu, D., Shen, D., Qin, M., Wu, S., Lin, F., Jang, S.-H., et al. (2020). Regulating Surface Termination for Efficient Inverted Perovskite Solar Cells with Greater Than 23% Efficiency. J. Am. Chem. Soc. *142*, 20134–20142. https://doi.org/10.1021/jacs.0c09845.

18. Stolterfoht, M., Caprioglio, P., Wolff, C.M., Márquez, J.A., Nordmann, J., Zhang, S., Rothhardt, D., Hörmann, U., Amir, Y., Redinger, A., et al. (2019). The impact of energy alignment and interfacial recombination on the internal and external open-circuit voltage of perovskite solar cells. Energy Environ. Sci. *12*, 2778–2788. https://doi.org/10.1039/C9EE02020A.

19. Li, D., Huang, Y., Wang, G., Lian, Q., Shi, R., Zhang, L., Wang, X., Gao, F., Kong, W., Xu, B., et al. (2021). Boosting the performance of MA-free inverted perovskite solar cells via multifunctional ion liquid. J. Mater. Chem. A Mater. *9*, 12746–12754. https://doi.org/10.1039/D1TA01883C.

20. Cacovich, S., Vidon, G., Degani, M., Legrand, M., Gouda, L., Puel, J.-B., Vaynzof, Y., Guillemoles, J.-F., Ory, D., and Grancini, G. (2022). Imaging and quantifying non-radiative losses at 23% efficient inverted perovskite solar cells interfaces. Nat. Commun. *13*, 2868. https://doi.org/10.1038/s41467-022-30426-0.

21. Wolff, C.M., Zu, F., Paulke, A., Toro, L.P., Koch, N., and Neher, D. (2017). Reduced Interface-Mediated Recombination for High Open-Circuit Voltages in CH3NH3PbI3 Solar Cells. Adv. Mater. *29*, 1700159. https://doi.org/10.1002/adma.201700159.

22. Wolff, C.M., Canil, L., Rehermann, C., Ngoc Linh, N., Zu, F., Ralaiarisoa, M., Caprioglio, P., Fiedler, L., Stolterfoht, M., Kogikoski, S., Jr., et al. (2020). Perfluorinated Self-Assembled Monolayers Enhance the Stability and Efficiency of Inverted Perovskite Solar Cells. ACS Nano *14*, 1445–1456. https://doi.org/10.1021/acsnano.9b03268.

23. Zhang, M., Chen, Q., Xue, R., Zhan, Y., Wang, C., Lai, J., Yang, J., Lin, H., Yao, J., Li, Y., et al. (2019). Reconfiguration of interfacial energy band structure for high-performance inverted structure perovskite solar cells. Nat. Commun. *10*, 4593. https://doi.org/10.1038/s41467-019-12613-8.

24. Zheng, X., Hou, Y., Bao, C., Yin, J., Yuan, F., Huang, Z., Song, K., Liu, J., Troughton, J., Gasparini, N., et al. (2020). Managing grains and interfaces via ligand anchoring enables 22.3%-efficiency inverted perovskite solar cells. Nat. Energy *5*, 131–140. https://doi.org/10.1038/s41560-019-0538-4.

25. Xing, Z., An, M.-W., Chen, Z.-C., Hu, M., Huang, X., Deng, L.-L., Zhang, Q., Guo, X., Xie, S.-Y., and Yang, S. (2022). Surface Re-Engineering of Perovskites with Buckybowls to Boost the Inverted-Type Photovoltaics. J. Am. Chem. Soc. *144*, 13839–13850. https://doi.org/10.1021/jacs.2c05235.

26. Belisle, R.A., Jain, P., Prasanna, R., Leijtens, T., and McGehee, M.D. (2016). Minimal Effect of the Hole-Transport Material Ionization Potential on the Open-Circuit Voltage of Perovskite Solar Cells. ACS Energy Lett. *1*, 556–560. https://doi.org/10.1021/acsenergylett.6b00270.

27. Zhuang, J., Mao, P., Luan, Y., Yi, X., Tu, Z., Zhang, Y., Yi, Y., Wei, Y., Chen, N., Lin, T., et al. (2019). Interfacial Passivation for Perovskite Solar Cells: The Effects of the Functional Group in Phenethylammonium Iodide. ACS Energy Lett. *4*, 2913–2921. https://doi.org/10.1021/acsenergylett.9b02375.

28. Zhang, C., Kong, W., Wu, T., Lin, X., Wu, Y., Nakazaki, J., Segawa, H., Yang, X., Zhang, Y., Wang, Y., and Han, L. (2021). Reduction of Nonradiative Loss in Inverted Perovskite Solar Cells by Donor−π–Acceptor Dipoles. ACS Appl. Mater. Interfaces *13*, 44321–44328. https://doi.org/10.1021/acsami.1c11683.

29. Degani, M., An, Q., Albaladejo-Siguan, M., Hofstetter, Y.J., Cho, C., Paulus, F., Grancini, G., and Vaynzof, Y. (2021). 23.7% Efficient inverted perovskite solar cells by dual interfacial modification. Sci. Adv. *7*, eabj7930. https://doi.org/10.1126/sciadv.abj7930.

30. Zhou, X., Zhang, L., Yu, J., Wang, D., Liu, C., Chen, S., Li, Y., Li, Y., Zhang, M., Peng, Y., et al. (2022). Integrated Ideal-Bandgap Perovskite/Bulk-Heterojunction Solar Cells with Efficiencies > 24. Adv. Mater. *34*, 2205809. https://doi.org/10.1002/adma.202205809.

31. Niu, Y., Peng, Y., Zhang, X., Ren, Y., Ghadari, R., Zhu, J., Tulloch, G., Zhang, H., Falaras, P., and Hu, L. (2022). Resonant Molecular Modification for Energy Level Alignment in Perovskite Solar Cells. ACS Energy Lett. *7*, 3104–3111. https://doi.org/10.1021/acsenergylett.2c01537.

32. Shin, D., Kang, D., Jeong, J., Park, S., Kim, M., Lee, H., and Yi, Y. (2017). Unraveling the Charge Extraction Mechanism of Perovskite Solar Cells Fabricated with Two-Step Spin Coating: Interfacial Energetics between Methylammonium Lead Iodide and C60. J. Phys. Chem. Lett. *8*, 5423–5429. https://doi.org/10.1021/acs.jpclett.7b02562.

33. Schulz, P., Edri, E., Kirmayer, S., Hodes, G., Cahen, D., and Kahn, A. (2014). Interface energetics in organo-metal halide perovskite-based photovoltaic cells. Energy Environ. Sci. *7*, 1377–1381. https://doi.org/10.1039/C4EE00168K.

34. Boehm, A.M., Liu, T., Park, S.M., Abtahi, A., and Graham, K.R. (2020). Influence of Surface Ligands on Energetics at FASnI3/C60 Interfaces and Their Impact on Photovoltaic Performance. ACS Appl. Mater. Interfaces *12*, 5209–5218. https://doi.org/10.1021/acsami.9b17535.

35. Schulz, P., Whittaker-Brooks, L.L., MacLeod, B.A., Olson, D.C., Loo, Y.-L., and Kahn, A. (2015). Electronic Level Alignment in Inverted Organometal Perovskite Solar Cells. Adv. Mater. Interfaces *2*, 1400532. https://doi.org/10.1002/admi.201400532.

36. Chen, S., Goh, T.W., Sabba, D., Chua, J., Mathews, N., Huan, C.H.A., and Sum, T.C. (2014). Energy level alignment at the methylammonium lead iodide/copper phthalocyanine interface. Apl. Mater. *2*, 081512. https://doi.org/10.1063/1.4889844.

37. Zu, F., Roß, M., Frohloff, L., Shin, D., Tessler, N., Albrecht, S., and Koch, N. (2022). Illumination-Driven Energy Level Realignment at Buried Interfaces between Organic Charge Transport Layers and a Lead Halide Perovskite. Sol. RRL *6*, 2101065. https://doi.org/10.1002/solr.202101065.

38. Chen, X., Wang, K., and Beard, M.C. (2019). Ultrafast probes at the interfaces of solar energy conversion materials. Phys. Chem. Chem. Phys. *21*, 16399–16407. https://doi.org/10.1039/C9CP02768H.

39. Yang, Y., Yang, M., Moore, D., Yan, Y., Miller, E., Zhu, K., and Beard, M. (2017). Top and bottom surfaces limit carrier lifetime in lead iodide

perovskite films. Nat. Energy *2*, 16207. https://doi.org/10.1038/nenergy.2016.207.

40. Yang, Y., Yan, Y., Yang, M., Choi, S., Zhu, K., Luther, J.M., and Beard, M.C. (2015). Low surface recombination velocity in solution-grown CH3NH3PbBr3 perovskite single crystal. Nat. Commun. *6*, 7961. https://doi.org/10.1038/ncomms8961.

41. Du, T., Kim, J., Ngiam, J., Xu, S., Barnes, P.R.F., Durrant, J.R., and McLachlan, M.A. (2018). Elucidating the Origins of Subgap Tail States and Open-Circuit Voltage in Methylammonium Lead Triiodide Perovskite Solar Cells. Adv. Funct. Mater. *28*, 1801808. https://doi.org/10.1002/adfm.201801808.

42. Palomares, E., Montcada, N.F., Méndez, M., Jiménez-López, J., Yang, W., and Boschloo, G. (2020). Chapter 7 - Photovoltage/photocurrent transient techniques. In Characterization Techniques for Perovskite Solar Cell Materials, M. Pazoki, A. Hagfeldt, and T. Edvinsson, eds. (Elsevier), pp. 161–180. https://doi.org/10.1016/B978-0-12-814727-6.00007-4.

43. Zheng, X., Troughton, J., Gasparini, N., Lin, Y., Wei, M., Hou, Y., Liu, J., Song, K., Chen, Z., Yang, C., et al. (2019). Quantum Dots Supply Bulk- and Surface-Passivation Agents for Efficient and Stable Perovskite Solar Cells. Joule *3*, 1963–1976. https://doi.org/10.1016/j.joule.2019.05.005.

44. Park, S.M., Abtahi, A., Boehm, A.M., and Graham, K.R. (2020). Surface Ligands for Methylammonium Lead Iodide Films: Surface Coverage, Energetics, and Photovoltaic Performance. ACS Energy Lett. *5*, 799–806. https://doi.org/10.1021/acsenergylett.0c00054.

45. Zu, F.-S., Amsalem, P., Salzmann, I., Wang, R.-B., Ralaiarisoa, M., Kowarik, S., Duhm, S., and Koch, N. (2017). Impact of White Light Illumination on the Electronic and Chemical Structures of Mixed Halide and Single Crystal Perovskites. Adv. Opt. Mater. *5*, 1700139. https://doi.org/10.1002/adom.201700139.

46. Cushman, C.V., Brüner, P., Zakel, J., Major, G.H., Lunt, B.M., Smith, N.J., Grehl, T., and Linford, M.R. (2016). Low energy ion scattering (LEIS). A practical introduction to its theory, instrumentation, and applications. Anal. Methods *8*, 3419–3439. https://doi.org/10.1039/C6AY00765A.

47. Lee, M., Choi, E., Soufiani, A.M., Lim, J., Kim, M., Chen, D., Green, M.A., Seidel, J., Lim, S., Kim, J., et al. (2021). Enhanced Hole-Carrier Selectivity in Wide Bandgap Halide Perovskite Photovoltaic Devices for Indoor Internet of Things Applications. Adv. Funct. Mater. *31*, 2008908. https://doi.org/10.1002/adfm.202008908.

48. Zhu, T., Zheng, D., Liu, J., Coolen, L., and Pauporté, T. (2020). PEAI-Based Interfacial Layer for High-Efficiency and Stable Solar Cells Based on a MACl-Mediated Grown FA0.94MA0.06PbI3 Perovskite. ACS Appl. Mater. Interfaces *12*, 37197–37207. https://doi.org/10.1021/acsami.0c09970.

49. Caprioglio, P., Stolterfoht, M., Wolff, C.M., Unold, T., Rech, B., Albrecht, S., and Neher, D. (2019). On the Relation between the Open-Circuit Voltage and Quasi-Fermi Level Splitting in Efficient Perovskite Solar Cells. Adv. Energy Mater. *9*, 1901631. https://doi.org/10.1002/aenm.201901631.

50. Ompong, D., Ram, K.S., Setsoafia, D.D.Y., Mehdizadeh Rad, H., and Singh, J. (2022). Saturation of Open-Circuit Voltage at Higher Light Intensity Caused by Interfacial Defects and Nonradiative Recombination Losses in Perovskite Solar Cells. Advanced Materials Interfaces *10*, 2201578. https://doi.org/10.1002/admi.202201578.

51. Zhou, M., Sarmiento, J.S., Fei, C., and Wang, H. (2019). Charge Transfer and Diffusion at the Perovskite/PCBM Interface Probed by Transient Absorption and Reflection. J. Phys. Chem. C *123*, 22095–22103. https://doi.org/10.1021/acs.jpcc.9b07591.

52. Shen, Q., Ogomi, Y., Chang, J., Tsukamoto, S., Kukihara, K., Oshima, T., Osada, N., Yoshino, K., Katayama, K., Toyoda, T., and Hayase, S. (2014). Charge transfer and recombination at the metal oxide/CH3NH3PbClI2/spiro-OMeTAD interfaces: uncovering the detailed mechanism behind high efficiency solar cells. Phys. Chem. Chem. Phys. *16*, 19984–19992. https://doi.org/10.1039/C4CP03073G.

53. Sandberg, O.J., Tvingstedt, K., Meredith, P., and Armin, A. (2019). Theoretical Perspective on Transient Photovoltage and Charge Extraction Techniques. J. Phys. Chem. C *123*, 14261–14271. https://doi.org/10.1021/acs.jpcc.9b03133.

54. Wheeler, S., Bryant, D., Troughton, J., Kirchartz, T., Watson, T., Nelson, J., and Durrant, J.R. (2017). Transient Optoelectronic Analysis of the Impact of Material Energetics and Recombination Kinetics on the Open-Circuit Voltage of Hybrid Perovskite Solar Cells. J. Phys. Chem. C *121*, 13496–13506. https://doi.org/10.1021/acs.jpcc.7b02411.

55. Maurano, A., Shuttle, C.G., Hamilton, R., Ballantyne, A.M., Nelson, J., Zhang, W., Heeney, M., and Durrant, J.R. (2011). Transient Optoelectronic Analysis of Charge Carrier Losses in a Selenophene/Fullerene Blend Solar Cell. J. Phys. Chem. C *115*, 5947–5957. https://doi.org/10.1021/jp109697w.

56. Glowienka, D., and Galagan, Y. (2022). Light Intensity Analysis of Photovoltaic Parameters for Perovskite Solar Cells. Adv. Mater. *34*, 2105920. https://doi.org/10.1002/adma.202105920.